



Cite this: *Catal. Sci. Technol.*, 2025, 15, 6884

# Optimizing the influential variables for enhanced photocatalytic performance of synergistic Ag–TiO<sub>2</sub>/FLG heterojunctions towards rapid mineralization of emerging polystyrene microplastics in water

Bhagyalakshmi Chinnam and Ramya Araga \*

The existence of microplastics (MPs) in marine and terrestrial environments is increasing tremendously. Due to their size (<5 mm), MPs could easily pass through the filtration processes of typical water treatment plants and ultimately reach surface water. Separation of MPs from aqueous media is expensive, and the treatment methods generally used for macro-plastic waste are unsuitable for MPs. Therefore, photocatalysis is an alternative technique to tackle environmental MP pollution. Though the photocatalytic degradation of various MPs has been reported, the effect of process parameters on photocatalytic degradation has not been investigated extensively. To fill this gap, the influence of various operating variables such as irradiation time, initial concentration of MPs, photocatalyst loading, initial pH, and reaction temperature on the photocatalytic degradation process of polystyrene (PS) MPs was investigated using a novel photocatalyst, *i.e.*, Ag<sup>+</sup> doped TiO<sub>2</sub>, heterojunctioned with few-layered graphene (ATG) under visible light irradiation. Further, photodegraded samples were analyzed using a nephelometer, FESEM, FTIR, XPS, TOC, GC-MS, and <sup>1</sup>H-NMR analyses to determine the effectiveness of the proposed photocatalyst. The results have revealed that visible-light-driven photocatalysis enhances PS polymeric chain scissions and reduces the concentration of PS MPs up to 63.28% within 120 h of irradiation. With a fixed amount of ATG, the increase in MP concentration decreased the degradation percentage. Similarly, the optimum ATG loading value with a pre-fixed MP concentration value improved the percentage mass loss. Further, ATG has exhibited a better performance at the pH value of 6.2 and ambient temperature.

Received 30th June 2025,  
Accepted 22nd September 2025

DOI: 10.1039/d5cy00792e

rsc.li/catalysis

## 1. Introduction

Few-layered graphene (FLG) is a two-dimensional carbon nanomaterial comprising a few stacked graphene sheets, typically ranging from 2 to 10 layers. It exhibits exceptional electrical, thermal, and mechanical properties, making it a promising candidate for a wide range of applications.<sup>1,2</sup> Photocatalysis is one among them that utilizes light to degrade several environmental contaminants,<sup>3</sup> including microplastics (MPs) suspended in the aqueous phase.

MPs are less than 5 mm in size and have a vast surface-to-volume ratio. Due to their chemical properties, MPs could adsorb hazardous substances from their adjacent environment.<sup>4,5</sup> On the other hand, MPs can serve as vectors for pathogens, bacteria, and viruses.<sup>6,7</sup> Further, these MPs, along with harmful contaminants and microbes, can enter the human body through lower trophic levels and threaten

human health.<sup>8–10</sup> The primary sources of MPs that enter the food chain are tap water,<sup>11</sup> bottled water,<sup>12</sup> and commercial salt.<sup>13</sup> Based on recent studies, an average human being's intake is 5 g of MPs per week, which is nearly equal to a debit card's weight.<sup>14</sup>

Polystyrene (PS) is a common type of MP found in the environment due to the low recycling rate worldwide.<sup>15</sup> Recent investigations reported that PS waste can generate MPs when exposed to sunlight.<sup>16,17</sup> Several studies proved that PS MPs could cause respiratory problems and even pass through human cells, creating hazardous effects.<sup>18–21</sup> Therefore, this drives an urgency to eradicate these MPs from aqueous media.

Traditional removal methods, such as filtration,<sup>22</sup> sedimentation,<sup>23,24</sup> bioremediation,<sup>25,26</sup> and chemical treatments,<sup>27</sup> often fall short due to their inefficiency, high operational costs, and secondary pollution risks. They rely on physical removal, which can result in MP accumulation in sludge or landfill disposal.<sup>28</sup> Alternatively, photocatalytic degradation, an advanced oxidation process that involves

Department of Chemical Engineering, National Institute of Technology Warangal, Telangana, India-506004. E-mail: ramyaaraga@nitw.ac.in; Tel: +91 870 246 2620

highly active radicals to break down MPs under light irradiation, has emerged as a promising solution.<sup>29</sup> Therefore, numerous researchers have proposed photocatalysis to degrade various MPs suspended in aquatic environments. TiO<sub>2</sub> is a widely used photocatalyst owing to its higher oxidizing power, chemical inertness, and water insolubility. However, it has two major limitations: 1) a larger bandgap<sup>30</sup> and 2) a shorter lifetime of photogenerated e<sup>-</sup>/h<sup>+</sup> pairs.<sup>31,32</sup> Thus, TiO<sub>2</sub> only facilitates UV light. To enhance the optical absorption of the TiO<sub>2</sub> photocatalyst in the visible region, its structure must be modified using different techniques such as doping, grafting, heterojunction, *etc.*<sup>33</sup> Comparatively, doping a noble metal ion into the TiO<sub>2</sub> lattice will substantially reduce its bandgap due to the plasmonic effect.<sup>34</sup> Some of the noble metals, such as Ag,<sup>35–39</sup> Au,<sup>40</sup> Pt,<sup>41,42</sup> Pd,<sup>43–45</sup> and Ru,<sup>46</sup> are incorporated into different photocatalysts to shift their absorption into the visible region. However, compared with other noble metals, silver (Ag) is commonly used as a dopant in photocatalysts, which is economically feasible in the photocatalytic degradation of a wide range of pollutants.

In the same way, employing heterojunctions in photocatalysis has been proven to be the most promising approach for preparing advanced photocatalysts because of their feasibility and effectiveness for the spatial separation of e<sup>-</sup>/h<sup>+</sup> pairs.<sup>47</sup> Several materials were used to generate heterojunctions, such as carbon nanotubes,<sup>38</sup> reduced graphene oxide,<sup>48</sup> MoS<sub>2</sub>,<sup>49</sup> Bi<sub>2</sub>O<sub>3</sub>,<sup>50</sup> WO<sub>3</sub>,<sup>51</sup> and g-C<sub>3</sub>N<sub>4</sub> (ref. 52 and 53) with various photocatalysts to reduce the recombination rate of the photo-induced charge carriers. These modification techniques ultimately enhance the effectiveness of the photocatalyst, which directly improves its performance in degrading emerging environmental pollutants using abundant visible light.

Therefore, the current study proposes a novel photocatalyst, Ag<sup>+</sup> doped TiO<sub>2</sub> heterojunctioned with FLG (ATG) nanocomposite, to degrade monodispersed PS MPs uniformly suspended in the aquatic environment. The ATG photocatalyst was synthesized through a simple and inexpensive sol-gel technique and characterized using FESEM, XRD, XPS, DRS, and BET. Later, we have investigated the effect of various operating parameters such as irradiation time, initial concentration of PS MPs, loading of ATG, initial pH, and reaction temperature on the performance of ATG to degrade the aqueous phase PS MPs utilizing cost-effective visible light. Further, photodegraded PS MP samples were examined using a nephelometer, FESEM, XPS, FTIR, GC-MS, TOC analyzer, and <sup>1</sup>H-NMR spectrometer to evaluate the effectiveness of ATG.

## 2. Materials and methods

### 2.1 Materials

Titanium(IV) isopropoxide (Ti{OCH(CH<sub>3</sub>)<sub>2</sub>}<sub>4</sub>, TTIP, 97 + %, Thermo Fisher Scientific India Pvt. Ltd.), silver nitrate (AgNO<sub>3</sub>, ≥99%, Sigma Aldrich), hydrochloric acid (HCl, extra

pure, Finar), and ethanol (EtOH, C<sub>2</sub>H<sub>5</sub>OH, 99.9%, RCP Distilleries India Pvt. Ltd.) were used as the TiO<sub>2</sub> precursor, Ag<sup>+</sup> precursor, catalyst, and solvent, respectively. Natural graphite flakes (grade: +32 mesh, Nickunj Eximp Entp P Ltd.) and propan-2-ol (CH<sub>3</sub>CH(OH)CH<sub>3</sub>, isopropanol, IPA, extra pure, Finar) were utilized to produce FLG. All the experiments were performed using deionized (DI) water.

### 2.2 Synthesis of FLG

FLG was synthesized through the liquid phase exfoliation (LPE) technique mentioned elsewhere.<sup>54</sup> Initially, 10 g of natural graphite flakes were mixed in a proportionate solution (100 mL) of IPA in DI water. Then, the mixture was sonicated using a probe sonicator (make: Hielscher; Model: UP200H) at a frequency of 50/60 Hz for 1 h in an ice bath. Sonication was carried out intermittently with 40% amplitude and stopped for 10 minutes for every 10 minutes of functioning to prevent solvent evaporation due to excess heat generation. During the sonication process, the pressure variations in the solvent stimulate the growth and collapse of the micron-sized bubbles that induce the exfoliation of the bulk graphite.<sup>55</sup> After the sonication, the solution was centrifuged at 500 rpm for 90 minutes using a fixed-angle rotor laboratory centrifuge (make: Eppendorf; Model: 5430 R). Then, the top 50% of the graphene dispersion was carefully pipetted using a fine pipette (100–1000 μl) and transferred into another centrifuge tube. Finally, the obtained graphene dispersion was centrifuged at 6000 rpm for 1 h to separate the FLG, which was further dried in an oven overnight at 80 °C to remove the moisture. The powdered FLG was then characterized using FESEM, HRTEM, and Raman analysis.

### 2.3 Synthesis of the photocatalyst

The ATG photocatalyst was prepared using a simple and cost-effective sol-gel technique reported by Chinnam *et al.*, with a slight modification.<sup>38</sup> Initially, FLG was uniformly distributed in ethanol through the probe sonication technique. Next, TTIP in ethanol (1:10 ratio) and three mol% of AgNO<sub>3</sub> in ethanol solutions were added dropwise to the FLG dispersion one after another while maintaining a constant stirring speed of 350 rpm. Later, HCl was added dropwise to the above solution. Finally, a gel was obtained after the dropwise addition of DI water, which was further dried overnight in an oven at 70 °C, and then calcined at 450 °C for 1 h in a muffle furnace with a ramp rate of 5 °C min<sup>-1</sup>. After that, the calcined photocatalyst was ground into powder and examined with a FESEM, XRD, BET analyzer, and UV/vis-DRS spectrometer to study the morphological and structural properties. In addition, we synthesized monodispersed PS MPs to evaluate the degradation performance of the prepared ATG photocatalyst. The detailed synthesis procedure and characterization results of PS MPs were described in our previous article.<sup>38</sup>

## 2.4 Photocatalytic degradation studies

Photocatalytic degradation studies were conducted in a custom-designed wooden chamber with dimensions of 45 cm × 40 cm × 30 cm in length, height, and width, respectively. A 50 W LED light (wavelength in the range of 400–800 nm, 5250 lm) was placed at the top of the reaction chamber. Firstly, a PS MP concentration of 0.05% w/v in 20 ml DI water was prepared and ultrasonicated for 10 min to obtain a uniformly dispersed suspension. Later, 5 mg (0.25 g L<sup>-1</sup>) of ATG photocatalyst was added to the PS suspension. Next, the reaction mixture was irradiated with light from a distance of 20 cm while continuously stirring at 300 rpm. At pre-defined time intervals, the reaction media were allowed to settle the ATG nanoparticles immediately at the bottom of the reactor flask. Later, the degraded MP suspension was separated and examined using a nephelometer, GC-MS, and <sup>1</sup>H-NMR spectrometer. Also, the diluted MP suspensions were assessed using a TOC analyzer. Moreover, MPs were separated from aqueous media & dried to characterize using FTIR. Finally, the procedure was repeated by varying process parameters such as irradiation time, initial PS MP concentration, ATG loading, initial pH, and reaction temperature.

## 2.5 Characterization techniques

Qualitative analysis of FLG was identified using Raman spectroscopy with a 532 nm excitation laser (make: Witec; Model: alpha 300) and HRTEM (make: Thermo Scientific; Model: Talos F200S G2). FLG and ATG morphological studies were performed using FESEM (make: JEOL; Model: JSM IT-800). A powder X-ray diffractometer (make: Panalytical; Model: X-pert powder) was employed to identify the phase and compute the structural properties of ATG. The optical spectrum of ATG was analyzed using a UV/vis-DRS spectrometer (make: Analytic Jena; Model: SPECORD-210 Plus) to estimate the bandgap. BET (Brunauer–Emmett–Teller) (make: Quantachrome instruments; Model: Autosorb IQ-MP-MP (2 stat.) Viton) was utilized to evaluate the specific surface area of the prepared photocatalyst. The turbidity of photodegraded PS MP suspensions was measured using a nephelometer (make: Hanna Instruments; Model: HI83414) to determine the concentration of PS MPs. The total organic carbon (TOC) content of the as-prepared and photodegraded MP suspensions was measured using a TOC analyzer (make: Shimadzu; Model: TOC-L CPN). Oxidative photocatalytic degradation was validated by identifying the functional groups of the PS MPs before and after the photodegradation process through ATR-FTIR (make: Bruker; Model: Alpha-II) analysis. The reaction medium (photodegraded MP suspension) was examined employing a GC-MS spectrometer (make: Agilent; Model: GC 8890/MS5977C/Autosampler7693A) to recognize the intermediate compounds of the photocatalytic degradation process. The <sup>1</sup>H-NMR spectrum of the photodegraded PS MP suspension was acquired through an NMR spectrometer (make: Bruker; Model: Avance III HD 400 MHz).

## 3. Results & discussion

### 3.1 Characterization of FLG

FLG was synthesized through LPE and characterized using FESEM, Raman spectroscopy, and HRTEM to examine the morphological and structural properties. Generally, LPE yields high purity of FLG in a smaller quantity.<sup>56</sup> A flaky structure of synthesized FLG with irregular size and shape was demonstrated in the FESEM image, as shown in Fig. 1(a). Raman analysis was performed to validate that the FLG has been exfoliated. The G and 2D bands were identified at 1580 and 2708 cm<sup>-1</sup>, respectively, as shown in Fig. 1(b). The G band is associated with the longitudinal optical phonon mode, representing in-plane vibrations of sp<sup>2</sup>-hybridized carbon atoms.<sup>57</sup> The 2D peak is a second-order dispersive Raman characteristic of the graphitic material correlated with the shape.<sup>58</sup> The D band appears at 1345 cm<sup>-1</sup>, indicating the edges of finite-size FLG and atomic defects within the layer. The relative intensity of D to G, *i.e.*,  $\left(\frac{I_D}{I_G}\right)$  determines the degree of disorder in the sample, which is evaluated as 0.34.<sup>59</sup> The lateral crystallite size ( $L_a$ ) was calculated as 56.25 nm using the expression below:<sup>60</sup>

$$L_a = (2.4 \times 10^{-10}) \lambda_1^4 \left( \frac{I_D}{I_G} \right)^{-1} \quad (1)$$

where  $\lambda_1$  is the wavelength of the excitation laser.

Fig. 1(c) illustrates the HRTEM micrograph of synthesized FLG. Observations validate that the LPE exfoliated FLG is likely in the form of a layered sheet with ~9 layers of graphene, where the distance between two layers is 0.335 nm. Fig. 1(d) shows the selected area electron diffraction (SAED) pattern, which discloses that the spots (0–110) and (–1010) are weaker than the spots (1–210) and (–2110), indicating the existence of FLG sheets.<sup>61,62</sup> Thus, these analyses confirm the quality of the synthesized FLG used in preparing the nanocomposite, ATG.

### 3.2 Characterization of ATG

The phase and crystalline properties of synthesized ATG were determined through XRD analysis. Fig. 2(a) demonstrates the diffraction spectrum of ATG, which confirms that the anatase phase prevails as the higher intensity peak is observed at a  $2\theta$  of 25.21° compared with the rutile phase peak at 27.18°. The diffraction peaks corresponding to silver and FLG indicate that adequate amounts of each material are augmented to host the photocatalyst TiO<sub>2</sub>. Further, the higher intensity diffraction peak corresponding to FLG ( $2\theta = 26.4^\circ$ ) in the ATG spectrum coincides with the major peak of TiO<sub>2</sub> ( $2\theta = 25.21^\circ$ ).<sup>63</sup> The crystallite size of the photocatalyst was calculated using the Debye–Scherrer equation mentioned below:

$$D = \frac{\kappa \lambda}{\beta \cos \theta} \quad (2)$$

where  $D$  is the crystalline size,  $\kappa$  is the Scherrer constant,  $\lambda$  is the X-ray wavelength, and  $\beta$  is the full-width half maximum

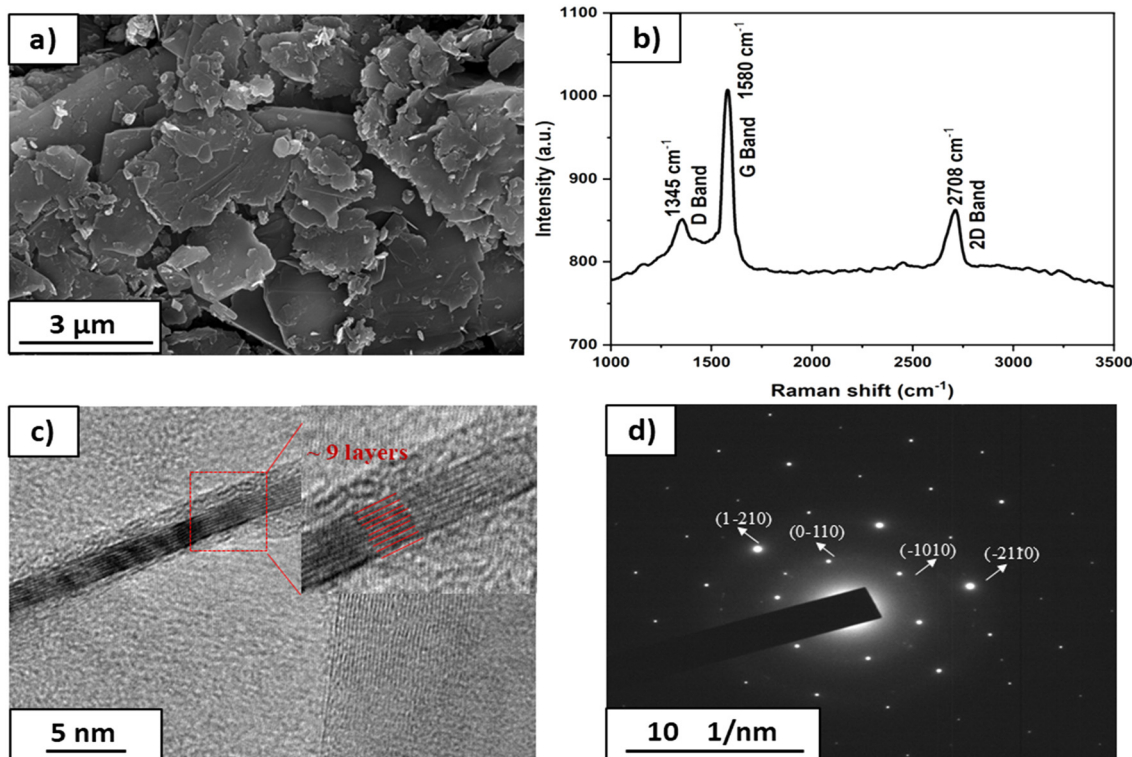


Fig. 1 a) FESEM image; b) Raman spectrum; c) HRTEM micrograph; and d) SAED pattern of synthesized FLG.

(FWHM) of the higher intensity peak. The evaluated crystallite size of ATG, the lattice parameters, and interplanar spacing are presented in Table 1.

The bandgap analysis of ATG was conducted through DRS reflectance spectroscopy, followed by Tauc's plot method as shown in Fig. 2(b). This method postulates that the absorption coefficient  $\alpha$  is associated with the bandgap,<sup>64</sup> as stated in eqn (3):

$$(\alpha \times hv)^n = A(hv - E_g) \quad (3)$$

where  $h$  is the Planck constant,  $\nu$  is the photon's frequency,  $E_g$  is the bandgap,  $A$  is a proportionality constant, and  $n$  is 2 for the direct bandgap and  $\frac{1}{2}$  for the indirect bandgap type semiconductors. According to Kubelka–Munk theory,<sup>65</sup> the above equation can be transformed into an equivalent reflectance spectrum for diffuse reflectance spectroscopy measurements as shown in eqn (4) and (5):

$$(f(R) \times hv)^n = A(hv - E_g) \quad (4)$$

$$f(R) = \frac{(1-R)^2}{2R} = \frac{\alpha}{S} \quad (5)$$

where  $S$  is the scattering coefficient and  $R$  is the absolute reflectance for the measured sample. As determined in Fig. 2(b), the bandgap of pristine anatase  $\text{TiO}_2$  was reduced significantly by doping silver ions into the lattice of  $\text{TiO}_2$  due to the inherent plasmonic nature of the noble metal silver.

Further, heterojunctions don't intrinsically decrease the bandgap of a semiconductor, they can influence the effective bandgap by developing a potential well that permits the tuning of electronic properties.<sup>66</sup> Moreover, the orientation and contact between the two materials in the heterojunction play a crucial role in effective spatial charge separation and bandgap reduction.<sup>51,67</sup> Therefore,  $\text{Ag}^+$  doping and FLG heterojunctions substantially reduced the bandgap of host photocatalyst  $\text{TiO}_2$  from 3.2 to 2.67 eV.

The  $\text{N}_2$  adsorption–desorption isotherm of ATG is displayed in Fig. 2(c). The surface area of nanoparticles plays an important role in photocatalysis. The BET-specific surface area of ATG was determined as  $65.26 \text{ m}^2 \text{ g}^{-1}$ , which is greater than that of commercially available  $\text{TiO}_2$ .<sup>68</sup> This ensures a higher contact area between the MPs and the photocatalyst, which improves the adsorption rate to enhance the performance of the photocatalyst.

Later, the morphology of the ATG photocatalyst was studied using FESEM. Fig. 3(a) shows the crystalline nanoparticles of ATG. Meanwhile, the energy dispersive X-ray spectroscopy (EDX) spectrum of ATG is shown in Fig. 3(b). The elemental analysis performed by EDX indicates the peaks corresponding to Ti, O, Ag, and C, which confirms that sufficient quantities of  $\text{Ag}^+$  and FLG are incorporated into  $\text{TiO}_2$ . Moreover, each element (Ti, O, Ag, and C) of the ATG nanocomposite was well distributed, as shown in Fig. 3(c).

Further, pristine  $\text{TiO}_2$  and ATG were examined using an XPS spectrometer, and the survey spectra are shown in Fig.

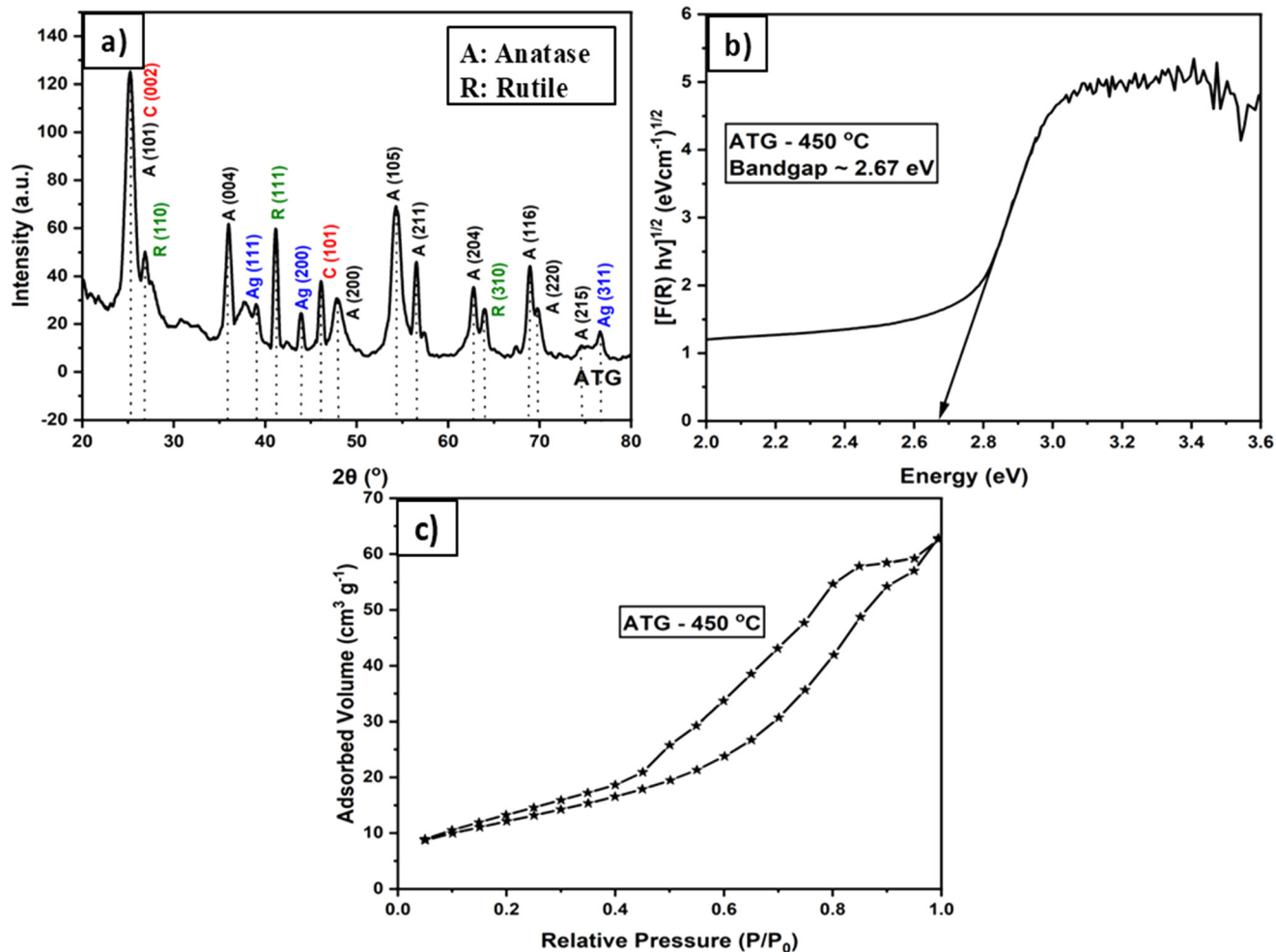


Fig. 2 a) XRD analysis; b) Tauc's plot corresponding to the reflectance spectrum; and c) N<sub>2</sub> adsorption-desorption isotherm of ATG.

Table 1 Structural properties of the synthesized ATG

Sample	$2\theta$ (°)	FWHM (°)	Crystallite size ( $D$ ) (nm)	Lattice parameter (Å)		Interplanar spacing ( $d$ ) (Å)
				$a = b$	$C$	
ATG	25.21	0.44	19.32	3.82	9.55	3.53

S1. The high-resolution spectra of Ti 2p, O 1s of TiO<sub>2</sub> and, Ti 2p, O 1s, Ag 3d, and C 1s of ATG are displayed in Fig. 4(a) to (f). Binding energies of Ti 2p<sub>3/2</sub> and Ti 2p<sub>1/2</sub> are detected at ~457.4 and ~463.1 eV, demonstrating the presence of the Ti<sup>4+</sup> state in both TiO<sub>2</sub> and ATG.<sup>69</sup> Likewise, the O 1s binding energy is observed at 528.5 eV due to the existence of O<sup>2-</sup> in both the TiO<sub>2</sub> and ATG lattices.<sup>70</sup> Meanwhile, in the case of ATG, deconvoluted binding energies of Ag 3d<sub>5/2</sub> and Ag 3d<sub>3/2</sub> are presented at peaks 371.5 and 365.6 eV, indicating the existence of Ag.<sup>71</sup> Similarly, the binding energy corresponding to the C 1s spectrum is observed at 284.5 and 287.3 eV. The first peak confirms the C-C & C=C bonds of FLG. The second peak indicates the inter-molecular interactions (due to heterojunctions) between Ag-TiO<sub>2</sub> & FLG. It also resembles

C=O & C-O bonds due to partial oxidization of FLG occurred during the calcination process.<sup>72,73</sup>

### 3.3 Photocatalytic degradation studies

**3.3.1 Impact of irradiation time.** The concentration (in % w/v) of the photodegraded PS MP suspension was evaluated using the turbidity calibration curve reported in our previous article.<sup>73</sup> In brief, known concentrations (0.01 to 0.08% w/v) of PS MPs dispersed in DI water were prepared and their turbidity was measured to plot the calibration curve. Turbidity analysis is a significantly used technique to estimate the percentage concentration of pollutants eliminated from the aquatic environment.<sup>74,75</sup> Fig. 5(a) shows the time-dependent photocatalytic

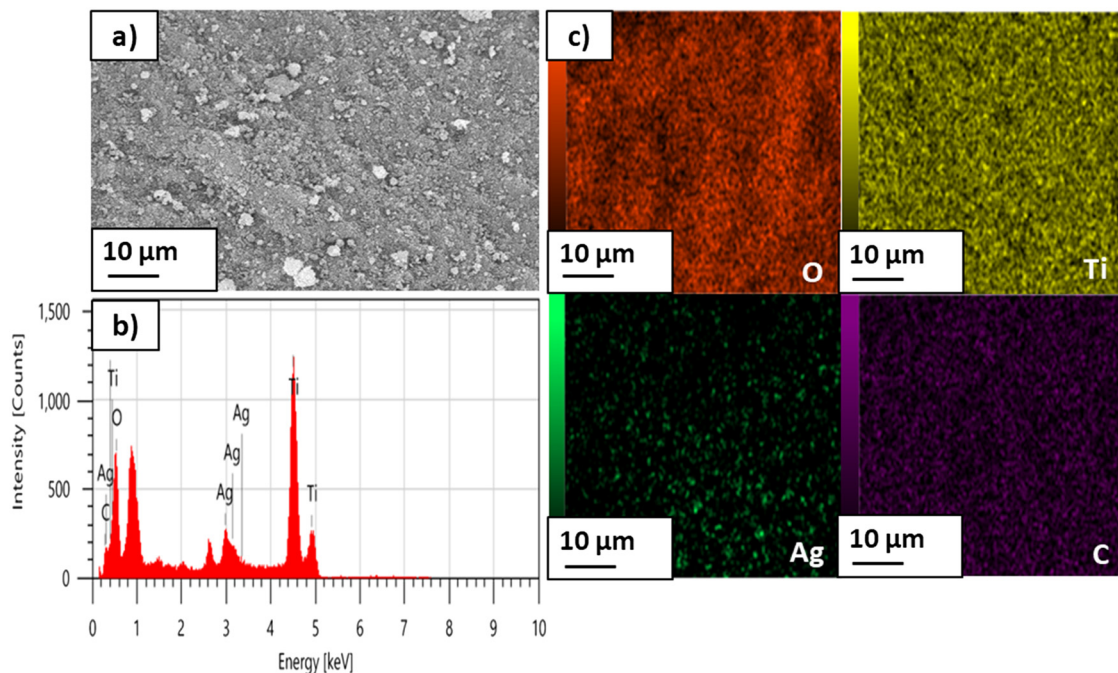


Fig. 3 a) FESEM image of ATG; b) EDAX analysis; and c) elemental mappings.

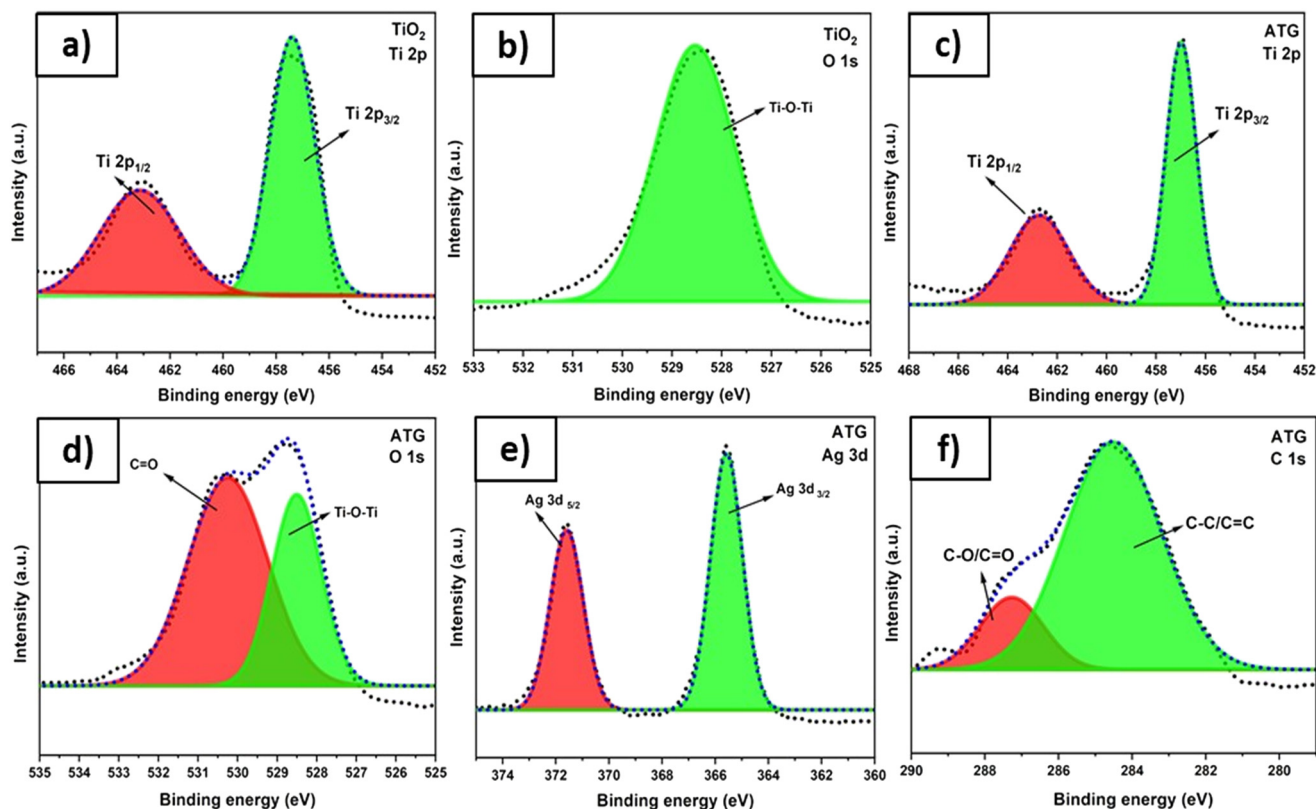


Fig. 4 XPS spectra of  $\text{TiO}_2$ : a) Ti 2p; & b) O 1s; and XPS spectra of ATG: c) Ti 2p; d) O 1s; e) Ag 3d; & f) C 1s.

degradation process of PS MPs in the presence of ATG. After 120 h of irradiation, the PS MP concentration was gradually reduced from 0.05 to 0.01833% w/v, yielding a

63.34% mass loss, where the % mass loss of the photocatalytic degradation process was calculated using the formula given below:

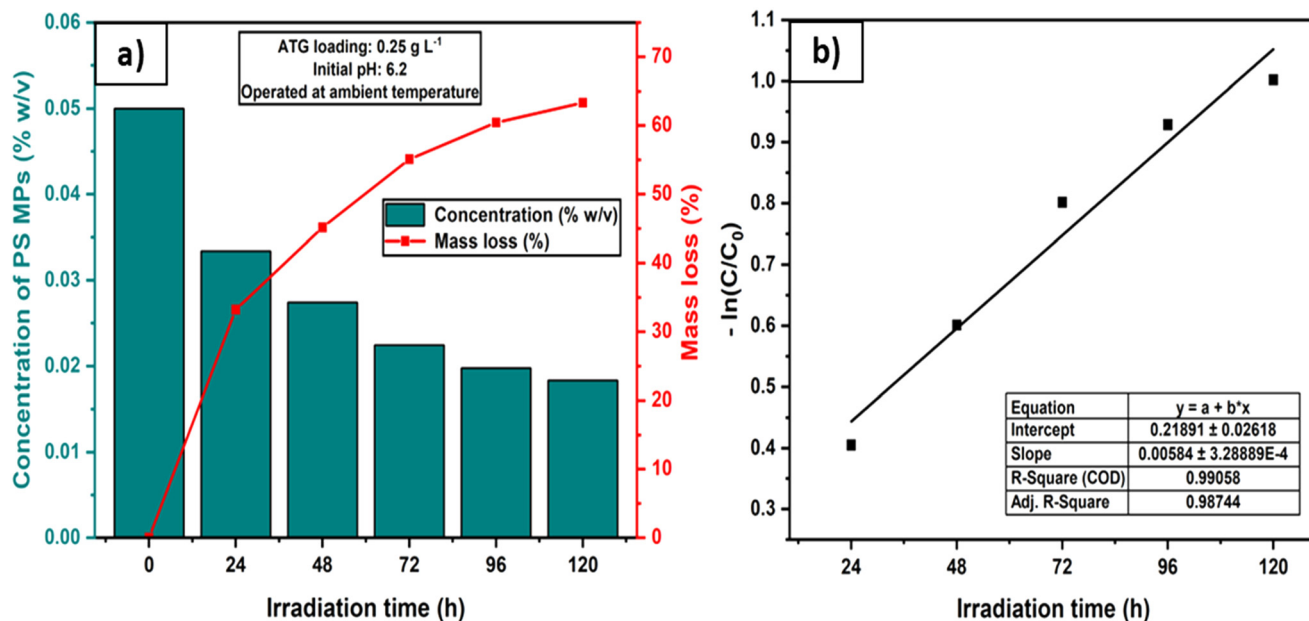


Fig. 5 a) Effect of irradiation time on photocatalytic degradation; b) rate constant plot.

% mass loss

$$= \frac{\text{Initial concentration of MPs} - \text{Final concentration of MPs}}{\text{Initial concentration of MPs}} \times 100 \quad (6)$$

After 96 h of irradiation, the slope rate of the percentage mass loss curve is minimal (2.88%, which is less than 5% even after 24 h of irradiation). Therefore, the optimum irradiation time for the described process is chosen as 96 h, beyond which the degradation rate is insignificant.

Fig. 5(b) shows the rate constant plot of the heterogeneous photocatalytic degradation process of PS MPs, acquired by first-order reaction kinetics as expressed in eqn (7):

$$-\ln \frac{C}{C_0} = kt \quad (7)$$

where  $C$  (%w/v) is the final concentration at the time  $t$  (h),  $C_0$  (%w/v) is the initial concentration, and  $k$  ( $\text{h}^{-1}$ ) is the reaction rate constant of the first-order.

Next, the as-prepared and photodegraded MP suspensions were diluted to determine the initial and final TOC contents ( $\text{TOC}_0$  &  $\text{TOC}$ ) to estimate fractional mineralization. The TOC value signifies the organic carbon related to PS polymeric chains and intermediates formed during oxidative photocatalytic degradation.<sup>76</sup> The reduction in TOC value imparts the partial mineralization of PS MPs. The PS MP suspension's true TOC value was gradually reduced from 787.8 to 495.6  $\text{mg L}^{-1}$  while increasing the irradiated time to

Table 2 Photocatalytic mineralization of PS MPs in the presence of ATG

Time (h)	0	24	48	72	96	120
TOC ( $\text{mg L}^{-1}$ )	787.8	693.7	621.4	563.3	516.5	495.6

120 h, as shown in Table 2. Therefore, it is confirmed that the photocatalytic degradation process of PS MPs produced the intermediate products, and part of them transformed into inorganic carbon due to PS polymeric chain scissions.

Later, photodegraded PS MPs were separated from the reaction media through centrifugal action and dried to identify the existing functional groups using FTIR analysis. Fig. 6(a) presents the associated FTIR spectra of the as-prepared and photodegraded PS MPs. By comparing both the FTIR spectra before and after the photocatalytic degradation, the identified new peaks from the wavenumbers of 800 to 1250  $\text{cm}^{-1}$  represent the stretching of the C=C bond, which indicates the existence of alkenes.<sup>38,77</sup> FTIR spectra were magnified to visualize the bands corresponding to the formation of alkenes as illustrated in Fig. 6(b). Likewise, new additional peaks in the region from 1300 to 1750  $\text{cm}^{-1}$  correspond to the formation of carbonyl functional groups (carboxylic acids (R-COOH), aldehydes (R-CHO), or ketones (R-(CO)-R)), which are displayed in Fig. 6(c).<sup>74,78</sup> Similarly, another set of new peaks at different wavenumbers in the region from 2150 to 2650  $\text{cm}^{-1}$  indicate C=C=O bond stretching, which implies the presence of ketenes on the PS polymeric chain, as shown in Fig. 6(d).<sup>77,79</sup>

The carbonyl index (CI) of the as-prepared and degraded PS MPs was evaluated using the carbonyl peak at 1603  $\text{cm}^{-1}$  and a reference peak (highly stable aromatic C-H bond) at 3057  $\text{cm}^{-1}$ .<sup>74,79</sup> The CI confirms the photochemical oxidation of unsaturated functional groups (C=C to C=O). The assessed values of CI are 0.26 and 0.54, corresponding to the as-prepared and photocatalytically degraded PS MPs, respectively.

Further, the as-prepared and photodegraded PS MPs were analysed using XPS to study the chemical changes occurred

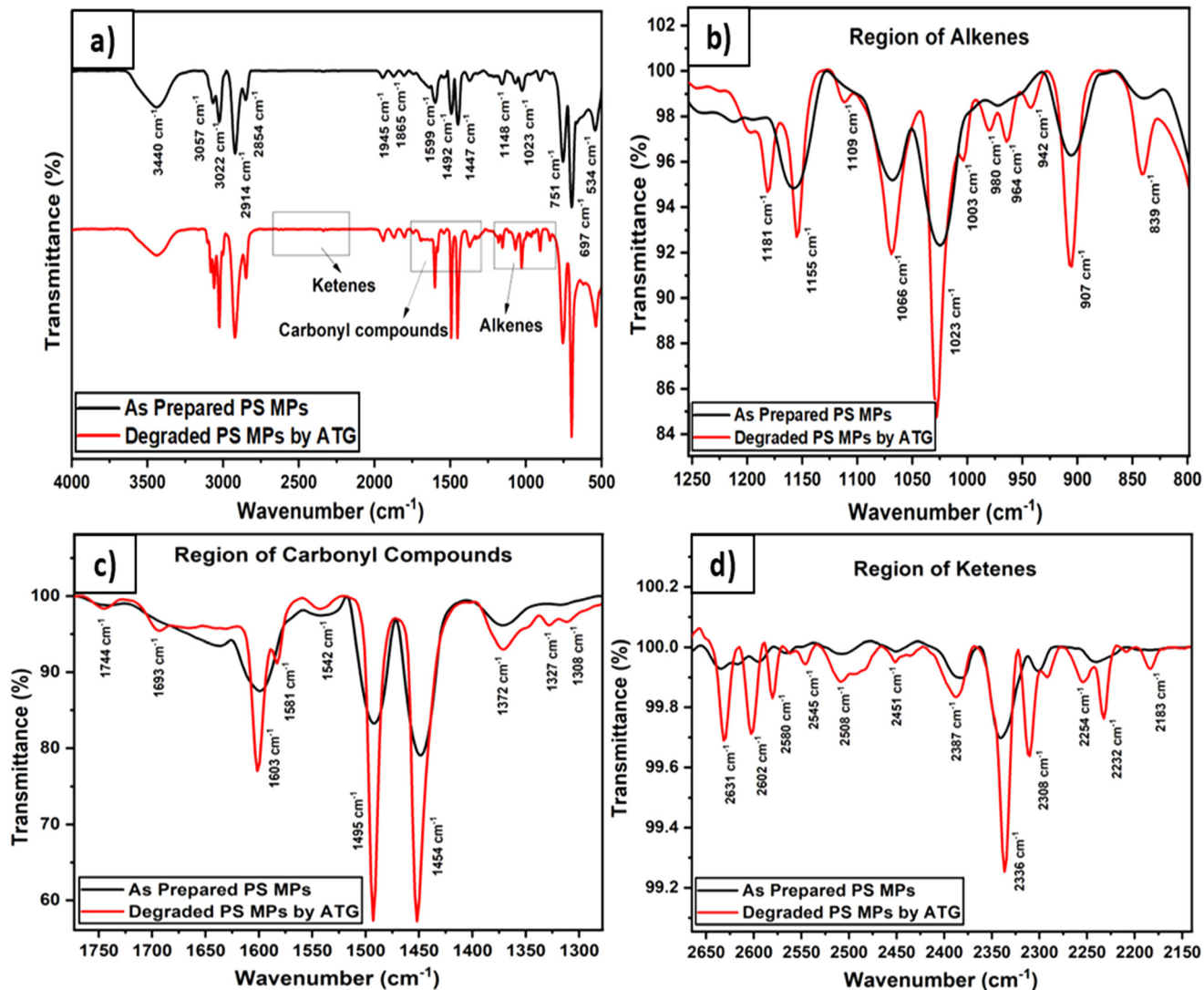


Fig. 6 FTIR spectra of the (a) as-prepared and photodegraded PS MPs; (b), (c), & (d) zoom of the spectra between 800 to 1250 cm<sup>-1</sup>, 1300 to 1750 cm<sup>-1</sup>, & 2150 to 2650 cm<sup>-1</sup>.

on the surface of MPs due to photodegradation. Fig. S2 demonstrates the survey spectra of both the as-prepared and photodegraded PS MPs. Fig. 7(a) to (d) show the C 1s and O 1s spectra of the as-prepared and degraded PS MPs. A single peak at 284.7 eV in the C 1s spectra of the as-prepared PS MPs is attributed to the C-C or C-H bonds of the polymer. Meanwhile, the binding energy at 286 eV indicates the formation of the C-O group in the C 1s spectra of degraded PS MPs.<sup>88</sup> Similarly, the binding energy of O 1s is detected at 532.2 eV, representing the presence of impure oxygen groups (C-O) on the surface of the as-prepared PS MPs. On the other hand, a new peak at 533.1 eV corresponds to the -COO group, which resembles the further oxidation of C-O to -COO in photodegradation of PS MPs.<sup>89</sup>

Furthermore, the morphological changes due to surface degradation of PS MPs were observed through FESEM analysis. Fig. 8(a) illustrates the as-prepared spherical shaped PS MPs and Fig. 8(b) and (c) confirm the surface

deterioration due to photodegradation of PS MPs. After 120 h of irradiation, we were unable to recognize the original spherical shape of MPs. Rather, EDAX analysis (shown in Fig. 8(d)) reveals the chemical composition of the material, thereby concluding the degraded PS MPs.

Finally, GC-MS analysis was performed to identify the potential intermediates of the oxidative degradation process, and the spectrum is displayed in Fig. 9. Exposure of ATG to visible light initiates the degradation process by producing e<sup>-</sup>/h<sup>+</sup> pairs in ATG. Later, photo induced e<sup>-</sup> will transfer to the conduction band, leaving h<sup>+</sup> in the valence band of ATG. Then, these e<sup>-</sup> and/or h<sup>+</sup> will generate highly active radicals *e.g.*, hydroxide and superoxide radicals (-OH and ·O<sub>2</sub><sup>-</sup>) by attacking adsorbed molecules on the surface of the ATG. Further, these radicals break down the PS polymer chains. In general, the degradation reaction mechanisms occur in several pathways due to numerous possibilities of bond breaking, which includes elimination or addition and/or recombination of

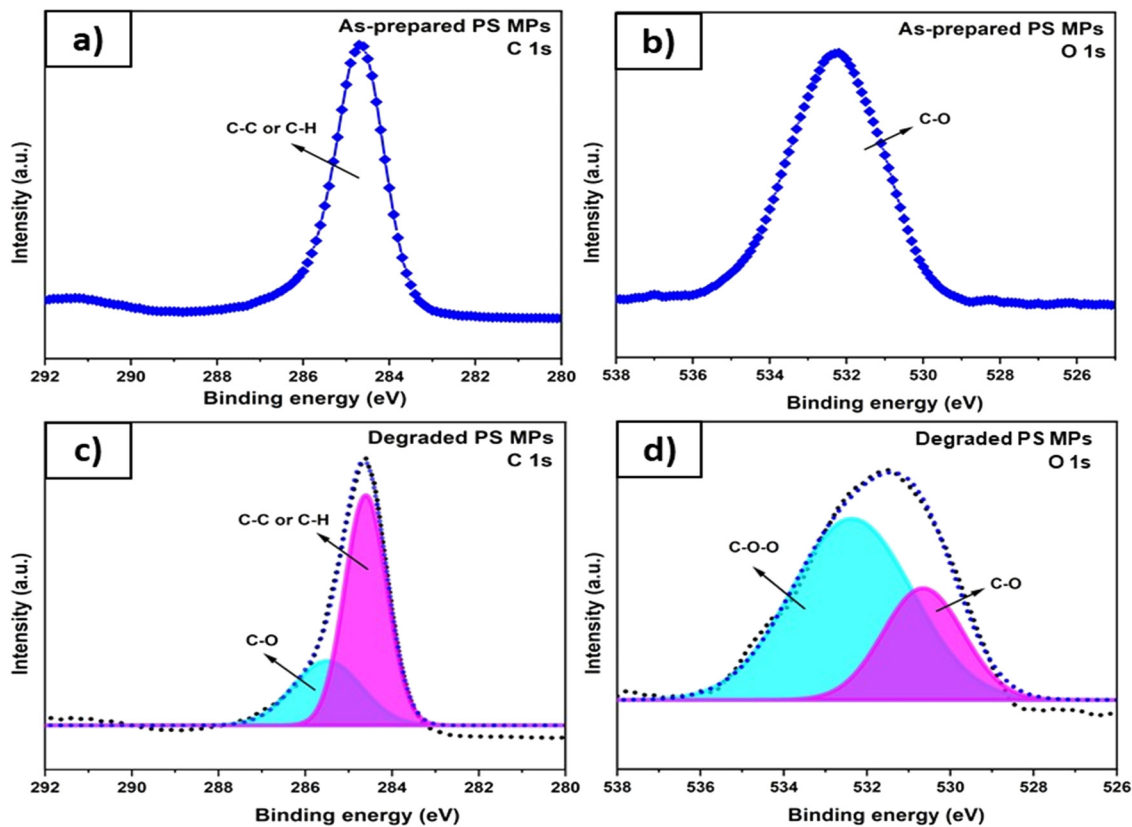


Fig. 7 XPS spectra of the as-prepared PS MPs: a) C 1s; & b) O 1s; and degraded PS MPs: c) C 1s; & d) O 1s.

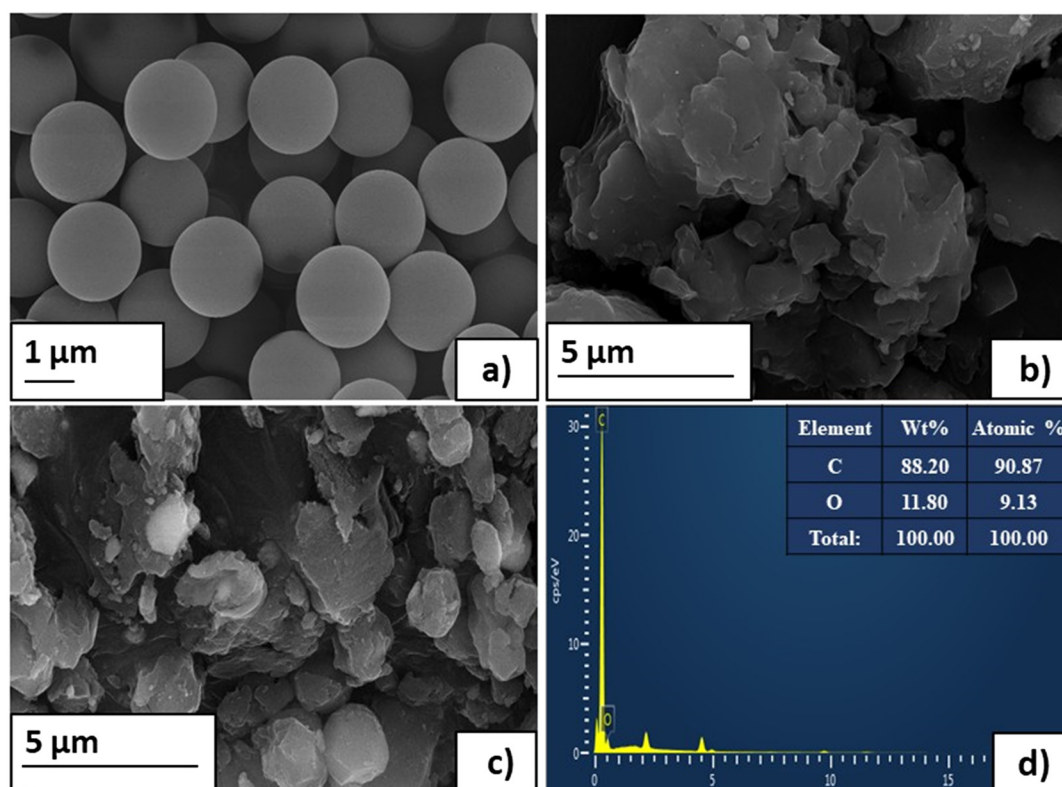


Fig. 8 FESEM images of a) as-prepared; b) and c) degraded PS MPs; and d) EDAX analysis of degraded PS MPs.

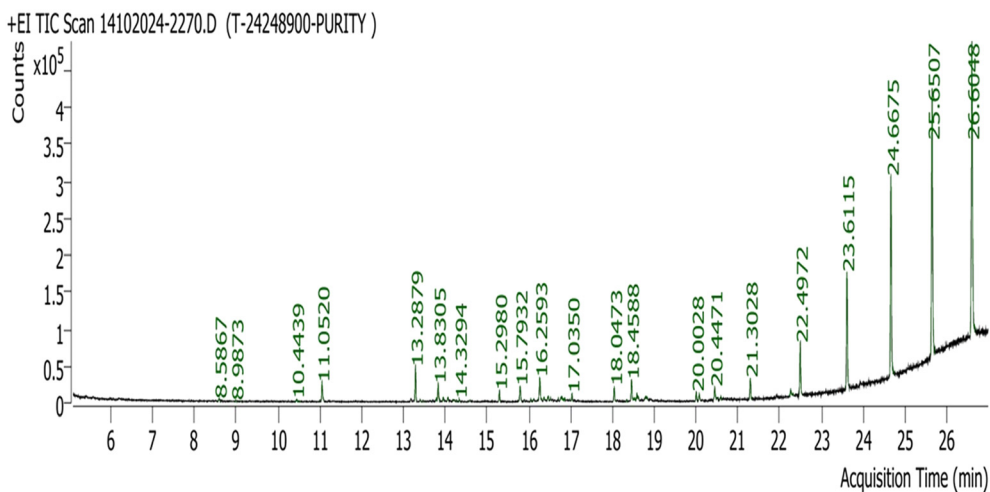


Fig. 9 GC-MS spectrum of photodegraded PS MPs after 120 h of irradiation.

various atoms. Table S1 shows the intermediate compounds produced during degradation and their concentration in the bulk sample. On keen observation of produced intermediates during the photocatalytic degradation process, and comparing them with other research studies (Acuña-Bedoya *et al.* 2021; Domínguez-Jaimes *et al.* 2021; Khairudin *et al.* 2022),<sup>74,75,78</sup> it is possible to confirm that  $\text{-O}_2^-$  plays probably a dominant role in the PS degradation mechanism.

Further, Table S1 also reveals the toxicity level of each intermediate product according to the Material Safety Data Sheet (MSDS). Most of the produced intermediates are either non-toxic or cause mild inflammation. Besides, 2,2-dimethylpentane is toxic as per MSDS, but its concentration is 0.07%, which is minute. However, PS MPs are comparatively more toxic than the detected intermediates, due to an extensive ecological influence and lifetime environmental & health effects as discussed earlier in section 1.

**3.3.2 Impact of PS MP concentration.** Once the irradiation time was optimized, the initial concentration of the PS MP suspension was altered to understand its effect on ATG performance. Other process parameters (irradiation time, ATG loading, initial pH, and reaction temperature) were remained unchanged at 96 h,  $0.25 \text{ g L}^{-1}$ , 6.2, and ambient. The PS MP concentration varied from 0.02 to 0.065% w/v, and the response plot is displayed in Fig. 10(a). The percentage degradation gradually increased from 0.02 to 0.03% w/v of the initial PS MP concentration as  $C$  is directly proportional to  $C_0$  according to eqn (6). Then, it decreased slowly from 0.03 to 0.065% w/v, as the increased initial PS MP concentration increased the turbidity of the reaction suspension, which obstructs the light from proceeding with further reactions.<sup>80</sup> Therefore, 0.03% w/v PS MP concentration is chosen as optimum, which yields 65.63% mass loss for this photocatalytic degradation system.

**3.3.3 Impact of ATG loading.** Similarly, to evaluate the effect of ATG loading on the photocatalytic degradation process, the amount of ATG was varied from 0.15 to 0.35 g

$\text{L}^{-1}$ . During this, an optimized irradiation time of 96 h and a PS MP concentration of 0.03% w/v were employed. Also, other reaction conditions, such as an initial pH of 6.2 and ambient reaction temperature, were maintained. Fig. 10(b) demonstrates the impact of ATG loading on the degradation of PS MPs suspended in aqueous media. The percentage degradation continued to increase as the ATG dosage increased. However, it increased rapidly from 0.15 to  $0.25 \text{ g L}^{-1}$  of ATG loading, and then there was an insignificant improvement in the percentage mass loss beyond  $0.25 \text{ g L}^{-1}$ . Given that, increasing ATG loading will increase the amount of light being scattered, which hinders the transmittance of light.<sup>81</sup> Thus,  $0.25 \text{ g L}^{-1}$  ATG loading is considered as the optimum for the described photocatalytic system.

**3.3.4 Impact of initial pH.** The initial pH of the PS MP suspension significantly controls the surface charge of the photocatalyst, which directly affects the performance of photocatalysis. To investigate this, photocatalytic degradation studies were conducted in an ambient atmosphere, at different initial pH values ranging from 4.5 to 9 while maintaining the optimized process conditions; the concentration of PS MPs at 0.03% w/v, ATG loading at  $0.25 \text{ g L}^{-1}$ , and an irradiation time of 96 h. The host material of ATG, *i.e.*,  $\text{TiO}_2$ , has superior oxidizing ability under acidic conditions; however, additional  $\text{H}^+$  ions might decrease the degradation rate.<sup>82</sup> The surface of ATG becomes protonated at acidic pH and initiates rivalry among MPs and  $\text{Cl}^-$  ions (coming from HCl) at the ATG's active sites.<sup>76</sup> Likewise, under alkaline conditions, the surface of ATG will be deprotonated, and it is incompatible with photocatalysis due to the repulsion of PS MPs at the negatively charged surface of ATG.<sup>83</sup> Fig. 10(c) shows the influence of initial pH on the photocatalytic degradation process of PS MPs. The degradation rate is enhanced from an acidic to a neutral pH of 6.2 and then diminished under alkaline conditions. Further, as the photocatalysis progresses, a reduction in the pH value of 0.3 to 0.4 is observed after 96 h of irradiation. This may be due to the

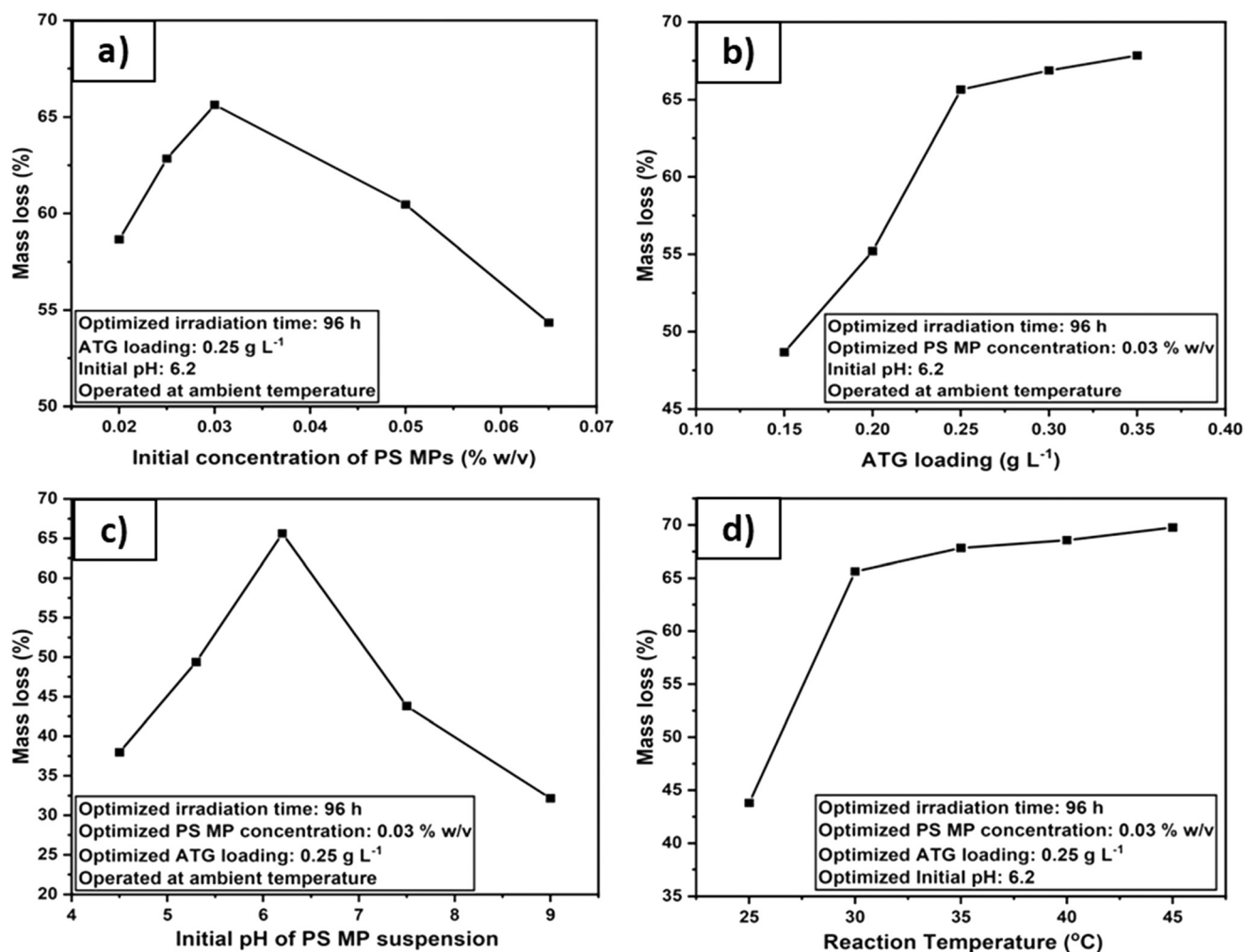


Fig. 10 Impact of a) initial PS MP concentration; b) ATG loading; c) initial pH; and d) reaction temperature on the photocatalytic degradation process.

acidic nature of the produced intermediates. Accordingly, MPs' optimum percentage mass loss will be obtained in the pH range of 6 to 6.6.

**3.3.5 Impact of reaction temperature.** Finally, to study the impact of the reaction temperature on the photocatalytic degradation of PS MPs, photocatalytic reactions were performed at various temperature values *i.e.*, 25, 30 (ambient temperature), 35, 40, and 45 °C while sustaining other reaction parameters: irradiation time, initial MP concentration, ATG dosage, and initial pH at their optimized values. Each pre-defined temperature was preserved uniformly during the degradation, using an orbital shaking incubator (Remi, CIS-24 plus). Generally, photocatalytic activity will be improved with reaction temperature. However, in the case of photocatalysis, a temperature rise beyond 80 °C is not favourable for the photocatalytic reactions to proceed, because it boosts the energy of the photoinduced excitons, which directly enhances the recombination rate of  $e^-/h^+$  pairs.<sup>82</sup> In the same way, additional activation energy is essential to initiate the photooxidation reactions if the process temperature is below 20 °C.<sup>84</sup> As a result, a

temperature range from 20 to 80 °C is appropriate for the most effective photocatalysis.<sup>85</sup> The ATG performance in terms of degrading PS MPs with temperature change is illustrated in Fig. 10(d). The mass loss percentage was continuously increased from 25 to 45 °C. Further, the degradation rate was sharper from 25 to 30 °C; a slight improvement in the percentage mass loss was observed up to 45 °C. Beyond 30 °C, the rate of degradation of MPs is insignificant when compared with the additional external energy supplied to maintain the photodegradation system at a specific temperature. Consequently, ambient atmospheric temperature is better for operating photocatalytic degradation, which is economically feasible for typical water treatment plants.

Apart from turbidity analysis, the effect of parameter variation on the photocatalytic degradation process of PS MPs is evaluated and validated through TOC analysis. Fig. S3 demonstrates the fractional mineralization of PS MPs through chain scissions during the photocatalytic degradation, performed at various reaction environments. Comparatively, TOC was reduced to an optimum lower value

in the case of 0.03% w/v PS MP concentration, 0.25 g L<sup>-1</sup> ATG loading, initial pH of 6.2, and ambient reaction temperature, which is in accordance with the turbidity analysis. Therefore, the combination of the above-mentioned values of different process variables yields the optimal degradation percentage of PS MPs, which is 65.63.

**3.3.6 <sup>1</sup>H-NMR analysis.** The <sup>1</sup>H-NMR spectrum of the photodegraded PS MP suspension under the optimized values of various parameters (*i.e.*, irradiation time, initial PS MP concentration, ATG loading, initial pH, and reaction temperature) was utilized to validate the final concentration obtained through turbidity analysis. The unknown concentration of the degraded PS MP suspension under optimized conditions was estimated using the NMR calibration curve presented in our earlier article.<sup>73</sup> Briefly, a set of known concentrations *i.e.*, 2, 4, 6, 8, and 10 mg of MPs in 20 mL of deionized water suspensions (0.01, 0.02, 0.03, 0.04, and 0.05% w/v) were prepared and 2 mL of each suspension was individually dissolved in 1 mL of CDCl<sub>3</sub> containing 0.03% v/v of TMS (internal standard reference with the chemical shift at 0.00 ppm). Next, the <sup>1</sup>H-NMR spectra of the above-prepared sample were acquired and analyzed using MestReNova 15.1 software. Later, an NMR calibration curve was plotted using an integral ratio ( $\frac{I}{I_{\text{std}}}$ ), where *I* and *I*<sub>std</sub> are the integrals of PS MPs and TMS obtained from the <sup>1</sup>H-NMR spectra) against each known concentration of PS MPs. Similarly, the <sup>1</sup>H-NMR spectrum of the photodegraded PS MP suspension was obtained and analyzed using MestReNova 15.1 software. After keen observation, the signals were assigned to corresponding chemical shifts.<sup>86,87</sup> Fig. 11 demonstrates the <sup>1</sup>H-NMR

spectrum of the photodegraded PS MP suspension along with the PS chemical structure. Under the optimized conditions, the degraded PS MP suspension concentration was determined as 0.01027%, yielding a degradation percentage of 65.76%. This value is in accordance with the percentage mass loss achieved from the turbidity analysis (65.63%).

Generally, the type of photocatalyst & its loading, the size & initial concentration of MPs, and the nature of light & exposure time influence the percentage degradation of MPs. Table 3 illustrates the comparative studies of ATG with other photocatalysts reported for the degradation of PS MPs suspended in water. It also discloses the influence of various parameters on degradation of PS MPs using different photocatalysts. Comparatively, ATG exhibited better performance *i.e.*, 65.63% degradation efficiency within 96 h of exposure to visible light. The synergistic effect of Ag<sup>+</sup> doping and the heterojunctions of FLG have boosted the performance of the ATG nanocomposite.

## 4. Conclusions

A novel photocatalyst, ATG, was synthesized using a simple and cost-effective sol-gel technique and characterized to analyze the morphological and structural properties. The combination of Ag<sup>+</sup> doping and FLG heterojunctions incorporated into pristine TiO<sub>2</sub> substantially decreased its bandgap. Thus, it facilitates inexpensive visible light to induce e<sup>-</sup>/h<sup>+</sup> pairs in ATG. Further, these excitons generate highly active radicals to degrade the PS MPs suspended in water. The effect of various process variables, *i.e.*, irradiation time, PS MP concentration, ATG loading, initial pH, and reaction

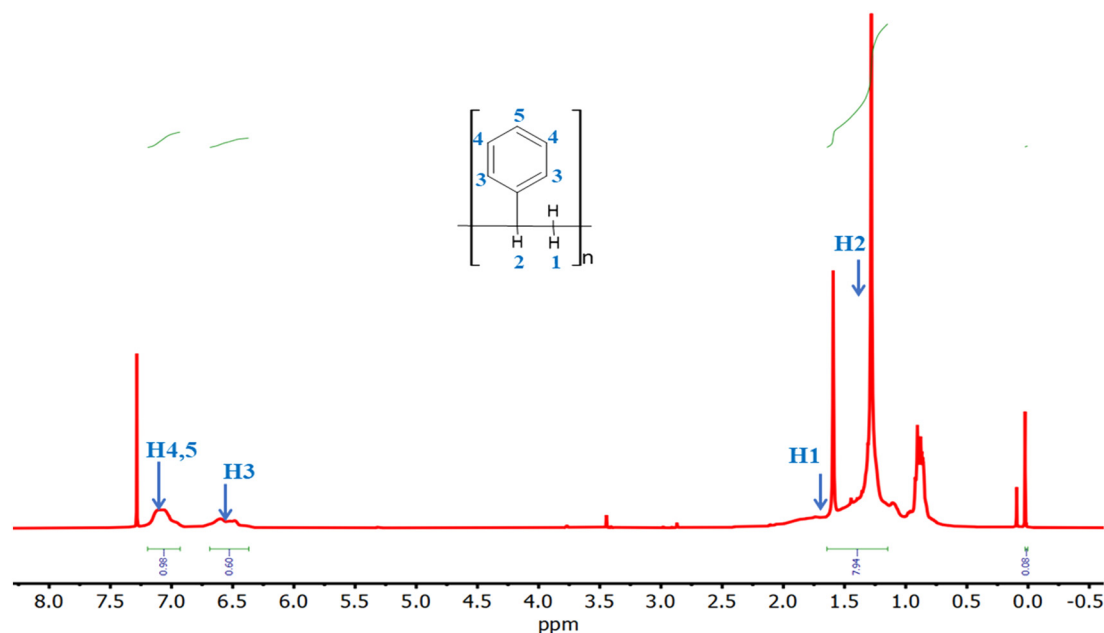


Fig. 11 <sup>1</sup>H-NMR spectrum of the degraded PS MP suspension under optimized conditions.

**Table 3** Comparative studies for the degradation of PS MPs using various photocatalysts

Photocatalyst	Light source	Initial PS MP concentration	Size of PS MPs	% degradation and irradiation time	Ref.
Cs <sub>3</sub> Bi <sub>2</sub> Br <sub>9</sub> /BiOCl	300 W Xe lamp	1 mg L <sup>-1</sup>	150 μm	42.3 ± 3.89% after 50 h	90
SnO <sub>2</sub> /g-C <sub>3</sub> N <sub>4</sub> /PVDF-HFP	1 sun; solar simulator (100 mW cm <sup>-2</sup> )	0.1 g L <sup>-1</sup>	100 nm	10.1% after 15 h	91
C-N-TiO <sub>2</sub>	50 W LED lamp (400–800 nm)	0.1 g L <sup>-1</sup>	1.04 μm	9% after 5 h	92
α-Fe <sub>2</sub> O <sub>3</sub> /g-C <sub>3</sub> N <sub>4</sub>	35 W Xe lamp	20 g L <sup>-1</sup>	278.6 nm	12.45% after 5 h	93
Flake-like BiOI-Fe <sub>3</sub> O <sub>4</sub> micro swimmer	50 W LED lamp (400–800 nm)	10 g L <sup>-1</sup>	150 μm	7.81% after 720 h	94
Anodized Cu <sub>2</sub> O/CuO	50 W LED lamp (400–800 nm)	50 mg L <sup>-1</sup>	1.1 μm	64% after 120 h	78
Anodized TiO <sub>2</sub>	50 W LED lamp (400–800 nm)	9 g L <sup>-1</sup>	350 nm	23% after 50 h	74
TiO <sub>2</sub> -P25/β-SiC foams	UV light (100–400 nm)	9 g L <sup>-1</sup>	314.8 nm	23.5% after 50 h	75
	UV-A light (320–400 nm)	0.3 g L <sup>-1</sup>	140 nm	29.2% after 7 h	76
			508 nm	16% after 7 h	
Triton X-100 based TiO <sub>2</sub>	UV light (254 nm)	1 mL of PS solution L <sup>-1</sup>	5 μm	44.66% after 12 h	94
Ag-TiO <sub>2</sub> /FLG nanocomposite	50 W LED lamp (400–800 nm)	0.3 g L <sup>-1</sup>	1.94 μm	65.63% in 96 h	Present work

temperature, on the photocatalytic degradation process was investigated thoroughly. The photocatalytic degradation was confirmed by examining the photodegraded PS MPs using a nephelometer, FESEM, XPS, GC-MS, FTIR, TOC analyzer, and <sup>1</sup>H-NMR spectrometer. The results have confirmed that ATG eliminated PS MPs by 63.28% in 120 h of visible light irradiation. Due to the sluggish kinetics of the photocatalytic degradation after 96 h, the process is diminished and optimized to an irradiation time of 96 h. Likewise, the MP concentration is reduced to 0.03% w/v, where the specific ATG loading has shown maximum degradation percentage. Similarly, ATG loading is maintained at 0.25 g L<sup>-1</sup> because the increased loading progresses with an insignificant reduction in mass loss. Finally, pH 6.2 and ambient temperature boosted the degradation of PS MPs to 65.63% in 96 h. Therefore, Ag<sup>+</sup> doping into the TiO<sub>2</sub> lattice and the heterojunction with FLG promotes the usage of visible light to produce e<sup>-</sup>/h<sup>+</sup> pairs, which further generate active radicals to degrade aqueous phase distributed PS MPs. These results conclude that the synthesized photocatalyst, ATG, can degrade PS MPs using visible light irradiation and establish adequate applications in the photocatalytic degradation of other harmful pollutants from aqueous media.

## Author contributions

Bhagyalakshmi Chinnam: conceptualization, methodology, investigation, validation, visualization, writing – original draft, and data curation. Ramya Araga: methodology, conceptualization, validation, supervision, resources, writing – review & editing, funding acquisition, and formal analysis.

## Conflicts of interest

The authors declare that no known competing financial or non-financial interests influence this research work.

## Data availability

Supplementary information is available. See DOI: <https://doi.org/10.1039/D5CY00792E>.

The data supporting this article have been included as part of the SI.

## Acknowledgements

The research discussed in this paper did not receive any grants from funding agencies in the commercial and non-profit sectors. We acknowledge the National Institute of Technology, Warangal, for providing the necessary research facilities. We also acknowledge the Indian Institute of Technology Hyderabad for performing TOC and XPS analyses. We thank the Centre for Nanotechnology, University of Hyderabad for assisting with the Raman analysis. Further, we recognize the QIMA Quality Inspection India PVT LTD and the Birla Institute of Technology and Science, Pilani – Goa Campus for conducting GC-MS and HRTEM analyses, respectively. Finally, we thank the Birla Institute of Technology and Science, Pilani – Hyderabad Campus for the execution of FESEM analysis.

## References

- G. Borand, N. Akçamlı and D. Uzunsoy, *Ceram. Int.*, 2021, **47**, 8044–8052.
- S. M. N. Sultana, E. Helal, G. Gutiérrez, E. David, N. Moghimian and N. R. Demarquette, *Crystals*, 2024, **14**, 687.
- Y. H. Li, Z. R. Tang and Y. J. Xu, *Chin. J. Catal.*, 2022, **43**, 708–730.
- W. Huang, B. Song, J. Liang, Q. Niu, G. Zeng, M. Shen, J. Deng, Y. Luo, X. Wen and Y. Zhang, *J. Hazard. Mater.*, 2021, **405**, 124187.
- Z. Chen, W. Sun, S. Wang, J. Yang, W. Huang, D. Huang, K. Jiang, X. Zhang and X. Sun, *Water Res.*, 2024, **267**, 122523.

- 6 D. N. Pham, L. Clark and M. Li, *J. Hazard. Mater. Lett.*, 2021, **2**, 100014.
- 7 Ü. N. Tavşanoğlu, G. Akca, T. Pekmez, G. Başaran Kankılıç, T. Çırak, A. S. Çağan, S. Ö. Kotiloğlu and H. P. Grossart, *Water Res.*, 2025, **274**, 123142.
- 8 M. Carbery, W. O'Connor and T. Palanisami, *Environ. Int.*, 2018, **115**, 400–409.
- 9 Z. Yuan, R. Nag and E. Cummins, *Sci. Total Environ.*, 2022, **823**, 153730.
- 10 H. Shao, Q. Wang, L. Wang, S. Dai, X. Ye and X. Z. Mao, *Water Res.*, 2025, **282**, 123635.
- 11 S. M. Mintenig, M. G. J. Löder, S. Primpke and G. Gerdt, *Sci. Total Environ.*, 2019, **648**, 631–635.
- 12 B. E. Oßmann, G. Sarau, H. Holtmannspötter, M. Pischetsrieder, S. H. Christiansen and W. Dicke, *Water Res.*, 2018, **141**, 307–316.
- 13 D. Peixoto, C. Pinheiro, J. Amorim, L. Oliva-Teles, L. Guilhermino and M. N. Vieira, *Estuar. Coast. Shelf Sci.*, 2019, **219**, 161–168.
- 14 K. Senathirajah, S. Attwood, G. Bhagwat, M. Carbery, S. Wilson and T. Palanisami, *J. Hazard. Mater.*, 2021, **404**, 124004.
- 15 S. Thakur, J. Chaudhary, B. Sharma, A. Verma, S. Tamulevicius and V. K. Thakur, *Curr. Opin. Green Sustainable Chem.*, 2018, **13**, 68–75.
- 16 K. Kik, B. Bukowska and P. Sicińska, *Environ. Pollut.*, 2020, **262**, 114297.
- 17 J. Lian, J. Wu, H. Xiong, A. Zeb, T. Yang, X. Su, L. Su and W. Liu, *J. Hazard. Mater.*, 2020, **385**, 121620.
- 18 L. Rubio, I. Bargailla, J. Domenech, R. Marcos and A. Hernández, *J. Hazard. Mater.*, 2020, **398**, 122900.
- 19 C. Cortés, J. Domenech, M. Salazar, S. Pastor, R. Marcos and A. Hernández, *Environ. Sci.: Nano*, 2020, **7**, 272–285.
- 20 C. Di Dong, C. W. Chen, Y. C. Chen, H. H. Chen, J. S. Lee and C. H. Lin, *J. Hazard. Mater.*, 2020, **385**, 121575.
- 21 Z. Yang, H. Wang, Y. Li and G. Zhang, *J. Colloid Interface Sci.*, 2025, **686**, 327–335.
- 22 Z. Wang, M. Sedighi and A. Lea-Langton, *Water Res.*, 2020, **184**, 116165.
- 23 B. Bayarkhuu and J. Byun, *Chemosphere*, 2022, **306**, 135572.
- 24 S. Zahmatkesh, J. J. Klemeš, A. Bokhari, C. Wang, M. Sillanpää, K. T. T. Amesho and M. Vithanage, *Int. J. Environ. Sci. Technol.*, 2023, **20**, 2229–2246.
- 25 X. L. Sun, H. Xiang, H. Q. Xiong, Y. C. Fang and Y. Wang, *Sci. Total Environ.*, 2023, **863**, 160953.
- 26 P. Masiá, D. Sol, A. Ardura, A. Laca, Y. J. Borrell, E. Dopico, A. Laca, G. Machado-Schiaffino, M. Díaz and E. Garcia-Vazquez, *Mar. Pollut. Bull.*, 2020, **156**, 111252.
- 27 K. Rajala, O. Grönfors, M. Hesampour and A. Mikola, *Water Res.*, 2020, **183**, 116045.
- 28 Q. Liu, Y. Chen, Z. Chen, F. Yang, Y. Xie and W. Yao, *Sci. Total Environ.*, 2022, **851**, 157991.
- 29 X. Liu, Z. Yang, H. Liu, Y. Li and G. Zhang, *J. Hazard. Mater.*, 2024, **480**, 136080.
- 30 I. Arora, H. Chawla, A. Chandra, S. Sagadevan and S. Garg, *Inorg. Chem. Commun.*, 2022, **143**, 109700.
- 31 H. Imahori, S. Kang, H. Hayashi, M. Haruta, H. Kurata, S. Isoda, S. E. Canton, Y. Infahsaeng, A. Kathiravan, T. Pascher, P. Chábera, A. P. Yartsev and V. Sundström, *J. Phys. Chem. A*, 2011, **115**, 3679–3690.
- 32 W. Gao, X. Zhao, C. Cui, X. Su, S. Zhang, X. Wang, X. L. Zhang, Y. Sang and H. Liu, *J. Alloys Compd.*, 2021, **862**, 158283.
- 33 L. Wang, J. Zhao, H. Liu and J. Huang, *J. Taiwan Inst. Chem. Eng.*, 2018, **93**, 590–602.
- 34 D. Dey, N. Halder, K. P. Misra, S. Chattopadhyay, S. K. Jain, P. Bera, N. Kumar and A. K. Mukhopadhyay, *Ceram. Int.*, 2020, **46**, 27832–27848.
- 35 I. Ellouzi, A. Bouddouch, B. Bakiz, A. Benlhachemi and H. Abou Oualid, *Chem. Phys. Lett.*, 2021, **770**, 138456.
- 36 F. Bensouici, T. Souier, A. A. Dakhel, A. Iratni, R. Tala-Ighil and M. Bououdina, *Superlattices Microstruct.*, 2015, **85**, 255–265.
- 37 S. Sen, S. Mahanty, S. Roy, O. Heintz, S. Bourgeois and D. Chaumont, *Thin Solid Films*, 2005, **474**, 245–249.
- 38 B. Chinnam, C. S. Dasagiri and R. Araga, *Environ. Sci. Pollut. Res.*, 2024, **31**, 32863–32874.
- 39 D. A. Maulana, M. Ibadurrohman and Slamet, *IOP Conf. Ser.: Mater. Sci. Eng.*, 2021, **1011**, 012054.
- 40 M. K. A. Mohammed, *Optik*, 2020, **223**, 165607.
- 41 T. S. Tofa, F. Ye, K. L. Kunjali and J. Dutta, *Catalysts*, 2019, **9**, 819.
- 42 D. Zhou, H. Luo, F. Zhang, J. Wu, J. Yang and H. Wang, *Adv. Fiber Mater.*, 2022, **4**, 1094–1107.
- 43 M. P. de la Flor, R. Camarillo, F. Martínez, C. Jiménez, R. Quiles and J. Rincón, *J. Environ. Chem. Eng.*, 2022, **10**, 107245.
- 44 W. Nabgan, B. Nabgan, T. A. Tuan Abdullah, M. Ikram, A. H. Jadhav, A. A. Jalil and M. W. Ali, *ACS Omega*, 2022, **7**, 3324–3340.
- 45 V. Inderan, N. A. S. Ahmad, N. A. M. Zaidi, N. Isa, W. Z. W. Kamis, H. L. Lee and S. Raseetha, *Malays. J. Anal. Sci.*, 2023, **27**, 54–62.
- 46 L. A. Ningsih, P. Y. Lu, S. Ashimura, M. Yoshida, W. C. Chen, Y. C. Chiu and C. Hu, *Chem. Eng. J.*, 2024, **480**, 148089.
- 47 J. Low, J. Yu, M. Jaroniec, S. Wageh and A. A. Al-Ghamdi, *Adv. Mater.*, 2017, **29**, 1–20.
- 48 M. H. Fadli, M. Ibadurrohman and S. Slamet, *IOP Conf. Ser.: Mater. Sci. Eng.*, 2021, **1011**, 012055.
- 49 X. Feng, R. Long, C. Liu and X. Liu, *Sep. Purif. Technol.*, 2022, **302**, 122138.
- 50 J. M. Musthafa and B. K. Mandal, *Opt. Mater.*, 2024, **154**, 115701.
- 51 X. Wang, Z. Zhu, J. Jiang, R. Li and J. Xiong, *Chemosphere*, 2023, **337**, 139206.
- 52 C. Zhang, L. Huang and A. Nekliudov, *Opt. Mater.*, 2024, **154**, 115786.
- 53 Y. Zhong, K. Liu, W. Chen and W. Lu, *Polymer*, 2022, **262**, 125495.

- 54 B. J. Akeredolu, I. Ahemen, A. N. Amah, A. D. Onojah, J. Shakya, H. N. Gayathri and A. Ghosh, *Heliyon*, 2024, **10**, e24964.
- 55 A. Ciesielski and P. Samori, *Chem. Soc. Rev.*, 2014, **43**, 381–398.
- 56 M. Zhou, T. Tian, X. Li, X. Sun, J. Zhang, P. Cui, J. Tang and L. C. Qin, *Int. J. Electrochem. Sci.*, 2014, **9**, 810–820.
- 57 A. Sethurajaperumal and E. Varrla, *ACS Sustainable Chem. Eng.*, 2022, **10**, 14746–14760.
- 58 D. L. Silva, J. L. E. Campos, T. F. D. Fernandes, J. N. Rocha, L. R. P. Machado, E. M. Soares, D. R. Miquita, H. Miranda, C. Rabelo, O. P. Vilela Neto, A. Jorio and L. G. Cançado, *Carbon*, 2020, **161**, 181–189.
- 59 M. S. Dresselhaus, A. Jorio and R. Saito, *Annu. Rev. Condens. Matter Phys.*, 2010, **1**, 89–108.
- 60 L. G. Cançado, K. Takai, T. Enoki, M. Endo, Y. A. Kim, H. Mizusaki, A. Jorio, L. N. Coelho, R. Magalhães-Paniago and M. A. Pimenta, *Appl. Phys. Lett.*, 2006, **88**, 12–14.
- 61 J. Geng, B. S. Kong, S. B. Yang and H. T. Jung, *Chem. Commun.*, 2010, **46**, 5091–5093.
- 62 A. Kaur and R. C. Singh, *Fullerenes, Nanotubes Carbon Nanostruct.*, 2017, **25**, 318–326.
- 63 M. Shabir, N. Shezad, I. Shafiq, I. M. Maafa, P. Akhter, K. Azam, A. Ahmed, S. H. Lee, Y. K. Park and M. Hussain, *J. Ind. Eng. Chem.*, 2022, **105**, 539–548.
- 64 P. Makuła, M. Pacia and W. Macyk, *J. Phys. Chem. Lett.*, 2018, **9**, 6814–6817.
- 65 R. López and R. Gómez, *J. Sol-Gel Sci. Technol.*, 2012, **61**, 1–7.
- 66 A. K. Sen Gupta, M. R. Hossan, N. K. Das, M. A. Matin and M. Quamruzzaman, 2023 6th Int. Conf. Electr. Inf. Commun. Technol. EICT 2023, 2023, 1–6.
- 67 A. Balapure, J. Ray Dutta and R. Ganesan, *RSC Appl. Interfaces*, 2024, **1**, 43–69.
- 68 M. Hussain, R. Ceccarelli, D. L. Marchisio, D. Fino, N. Russo and F. Geobaldo, *Chem. Eng. J.*, 2010, **157**, 45–51.
- 69 L. M. Santos, W. A. Machado, M. D. França, K. A. Borges, R. M. Paniago, A. O. T. Patrocinio and A. E. H. Machado, *RSC Adv.*, 2015, **5**, 103752–103759.
- 70 Y. An, J. Hou, Z. Liu and B. Peng, *Mater. Chem. Phys.*, 2014, **148**, 387–394.
- 71 J. Zhu, D. Wu, P. Liang, X. Zhou, Z. Peng, X. Chao and Z. Yang, *J. Alloys Compd.*, 2021, **856**, 2–9.
- 72 X. Zhang, S. Cao, Z. Wu, S. Zhao and L. Piao, *Appl. Surf. Sci.*, 2017, **402**, 360–368.
- 73 B. Chinnam and R. Araga, *Water, Air, Soil Pollut.*, 2025, **236**, 1–17.
- 74 J. D. Acuña-Bedoya, E. Luévano-Hipólito, E. I. Cedillo-González, L. P. Domínguez-Jaimes, A. M. Hurtado and J. M. Hernández-López, *J. Environ. Chem. Eng.*, 2021, **9**, 106208.
- 75 L. P. Domínguez-Jaimes, E. I. Cedillo-González, E. Luévano-Hipólito, J. D. Acuña-Bedoya and J. M. Hernández-López, *J. Hazard. Mater.*, 2021, **413**, 125452.
- 76 P. H. Allé, P. Garcia-Muñoz, K. Adouby, N. Keller and D. Robert, *Environ. Chem. Lett.*, 2021, **19**, 1803–1808.
- 77 P. García-Muñoz, P. H. Allé, C. Bertoloni, A. Torres, M. U. De La Orden, J. M. Urreaga, M. A. Dziurla, F. Fresno, D. Robert and N. Keller, *J. Environ. Chem. Eng.*, 2022, **10**, 108195.
- 78 K. Khairudin, N. F. Abu Bakar and M. S. Osman, *J. Environ. Chem. Eng.*, 2022, **10**, 108275.
- 79 A. Torikai, T. Takeuchi and K. Fueki, *Polym. Photochem.*, 1983, **3**, 307–320.
- 80 K. M. Reza, A. Kurny and F. Gulshan, *Appl. Water Sci.*, 2017, **7**, 1569–1578.
- 81 H. M. Coleman, V. Vimonses, G. Leslie and R. Amal, *J. Hazard. Mater.*, 2007, **146**, 496–501.
- 82 A. Kumar, *Int. J. Mater. Sci. Eng.*, 2017, **1**, 106–114.
- 83 S. Mozia, A. W. Morawski, M. Toyoda and M. Inagaki, *Desalination*, 2009, **241**, 97–105.
- 84 A. C. M. Fong and B. Fong, Proc. Int. Symp. Consum. Electron. ISCE, 2011, 18–19.
- 85 G. Mamba, M. A. Mamo, X. Y. Mbianda and A. K. Mishra, *Ind. Eng. Chem. Res.*, 2014, **53**, 14329–14338.
- 86 N. Peez, M. C. Janiska and W. Imhof, *Anal. Bioanal. Chem.*, 2019, **411**, 823–833.
- 87 G. Papini, G. Petrella, D. O. Cicero, C. Boggione and A. Rakaj, *Mar. Pollut. Bull.*, 2024, **198**, 115784.
- 88 O. M. Ba, P. Marmey, K. Anselme, A. C. Duncan and A. Ponche, *Colloids Surf., B*, 2016, **145**, 1–7.
- 89 L. Zan, S. Wang, W. Fa, Y. Hu, L. Tian and K. Deng, *Polymer*, 2006, **47**, 8155–8162.
- 90 X. Zhang, M. Zhang, C. Luo, Y. Li, L. Zhang, C. Li, X. Zhang, J. Liao and W. Zhou, *Appl. Catal., B*, 2025, **371**, 125288.
- 91 A. Fazli, S. Lauciello, R. Brescia, R. Carzino, A. Athanassiou and D. Fragouli, *Appl. Catal., B*, 2024, **353**, 124056.
- 92 A. D. Vital-Grappin, M. C. Ariza-Tarazona, V. M. Luna-Hernández, J. F. Villarreal-Chiu, J. M. Hernández-López, C. Siligardi and E. I. Cedillo-González, *Polymers*, 2021, **13**, 1–18.
- 93 C. Chai, H. Liang, R. Yao, F. Wang, N. Song, J. Wu and Y. Li, *Environ. Sci. Pollut. Res.*, 2023, **30**, 121702–121712.
- 94 I. Nabi, A. U. R. Bacha, K. Li, H. Cheng, T. Wang, Y. Liu, S. Ajmal, Y. Yang, Y. Feng and L. Zhang, *iScience*, 2020, **23**, 101326.